

---

Faculty of Science

Faculty Publications

---

Near-vent chemical processes in a hydrothermal plume: Insights from an integrated study of the Endeavour segment

L.A. Coogan, A. Attar, S.F. Mihaly, M. Jeffries & M. Pope

2017

This article can be found online at:

<https://doi.org/10.1002/2016GC006747>

---

Citation for this paper:

Coogan, L.A., Attar, A., Mihaly, S.F., Jeffries, M. & Pope, M. (2017). Near-vent chemical processes in a hydrothermal plume: Insights from an integrated study of the Endeavour segment. *Geochemistry, Geophysics, Geosystems*, 18, 1641-1660.  
<https://doi.org/10.1002/2016GC006747>



## RESEARCH ARTICLE

10.1002/2016GC006747

## Key Points:

- Temperature and light attenuation anomalies in the water column suggest ~50% of the hydrothermal heat flux is from diffuse flow
- Hydrothermal sediment accumulation rates drop dramatically within hundreds of meters of the major vent fields
- Hydrothermal sediment composition changes substantially with distance from the vents

## Supporting Information:

- Supporting Information S1
- Table S1

## Correspondence to:

L. A. Coogan,  
lacoogan@uvic.ca

## Citation:

Coogan, L. A., A. Attar, S. F. Mihalý, M. Jeffries, and M. Pope (2017), Near-vent chemical processes in a hydrothermal plume: Insights from an integrated study of the Endeavour segment, *Geochem. Geophys. Geosyst.*, 18, 1641–1660, doi:10.1002/2016GC006747.

Received 23 NOV 2016

Accepted 26 MAR 2017

Accepted article online 3 APR 2017

Published online 21 APR 2017

Corrected 18 MAY 2017

This article was corrected on 18 MAY 2017. See the end of the full text for details.

## Near-vent chemical processes in a hydrothermal plume: Insights from an integrated study of the Endeavour segment

L. A. Coogan<sup>1</sup> , A. Attar<sup>1</sup> , S. F. Mihalý<sup>2</sup> , M. Jeffries<sup>2</sup> , and M. Pope<sup>1</sup>
<sup>1</sup>School of Earth and Ocean Sciences, University of Victoria, Victoria, British Columbia, Canada, <sup>2</sup>Ocean Networks Canada, University of Victoria, Victoria, British Columbia, Canada

**Abstract** The Endeavour segment of the Juan de Fuca mid-ocean ridge is one of the best studied ridge segments and has recently been instrumented as part of Ocean Networks Canada's NEPTUNE cabled observatory. Here we investigate the interaction between high-temperature vent fluids and the overlying water column. A new tow-yo survey found that the average temperature anomaly in the neutrally buoyant plume was ~0.043°C. The water column temperature and light attenuation anomalies correlate linearly in some areas of the plume but in other areas there is a low light attenuation anomaly relative to the temperature anomaly. This temperature excess is interpreted to reflect heat input through (particle-poor) diffuse flow. If this is correct, about half of the heat flux along the Endeavour segment comes from diffuse flow. Sediment trap and push core data show that the mass accumulation rate of the hydrothermal component of the sediments decreases rapidly with distance from the major vent fields. Large changes in the composition of the hydrothermal component of the sediments also occur with distance from the vent fields. The composition of the sediments indicates (i) sulfides precipitate early and accumulate most rapidly close to the vents with a preferential order of element removal from the plume of  $Cd > Ag > Cu > Co \sim Fe$ ; (ii) barite is deposited somewhat further from the vents. Strontium and Pb appear to be strongly incorporated in barite and/or other sulfate minerals; (iii) at most a few percent of the mass of these "insoluble" elements that is vented gets deposited within 1.5 km of the vents.

## 1. Introduction

Since the discovery of hydrothermal vents along mid-ocean ridges, it has been apparent that the geochemical fluxes from these systems could play an important role in ocean biogeochemical cycles and hence the evolution of the earth system. There has been a lot of work investigating the composition of high-temperature vent fluids and the flux of these fluids [e.g., reviews by Von Damm, 1995; German and Seyfried, 2014]. Thermally constrained fluid fluxes have been combined with vent fluid compositions to determine geochemical fluxes associated with mid-ocean ridge hydrothermal systems [e.g., Elderfield and Schultz, 1996]. More recently, internally consistent hydrothermal fluxes have been estimated using both the compositions of hydrothermal fluids and altered rocks [Coogan and Dosso, 2012]. However, fluxes of elements into and out of the ocean associated with mid-ocean ridge hydrothermal systems are not simply determined from high-temperature vent fluid fluxes and compositions due to (i) formation of particulates in the water column during mixing between vent fluid and the overlying ocean; (ii) subsurface mixing and conductive cooling leading to nonconservative behavior during the formation of diffuse flow fluids; and (iii) element precipitation into, and leaching from, chimney structures. Quantifying the net geochemical fluxes into the ocean requires these processes be understood.

As high-temperature hydrothermal fluids vent into the ocean, they mix rapidly with surrounding water, cooling and increasing their pH, leading to the precipitation of particulates from the mixed fluid [e.g., Feely et al., 1987; Mottl and McConachy, 1990; Lilley et al., 1995; German and Seyfried, 2014]. This mixing, along with entrainment of particle-poor, low-temperature, diffuse fluid leads to the formation of a buoyant plume that rises until it reaches a level of neutral buoyancy and then spreads laterally. The composition of particulates formed within the plume depends on the initial composition of the vent fluid and seawater, the relative amounts of these end-members during particulate formation (or vent fluid dilution factor), and any subsequent scavenging of elements from the plume waters. Generally, metal sulfides form early, and

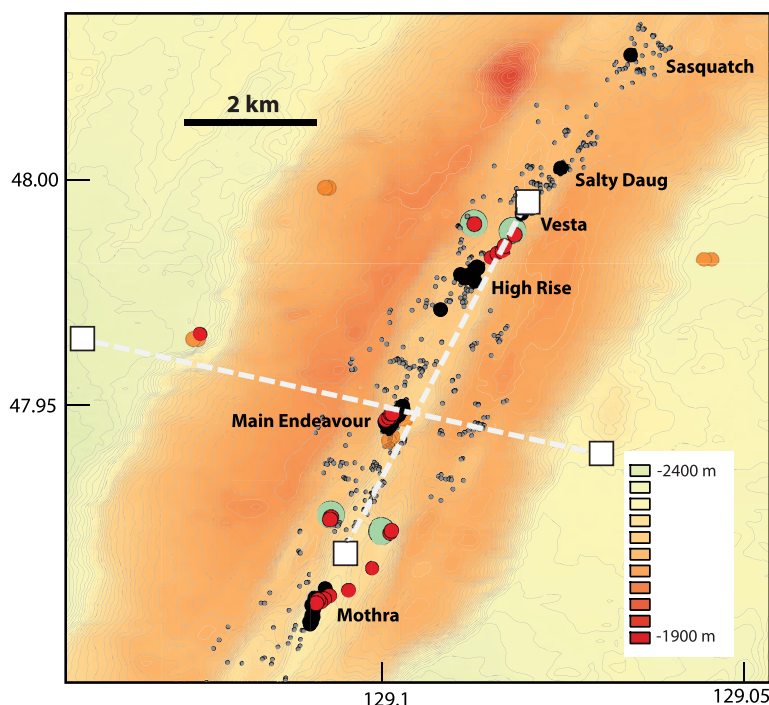


**Figure 1.** Location map showing the locations of sediment core samples (red circles are from this study and orange from Hrischeva and Scott [2007]), the major high-temperature vent fields (black circles; from geomapapp) and their names, the tow-yo survey lines (white dashed lines), the water column mooring locations (green circles) and the active and inactive sulfide mound locations (grey circles) from Jamieson et al. [2014].

Fe-oxyhydroxides and Mn-oxides later, although the relative importance of Fe-sulfides and Fe-oxides depends on the Fe/H<sub>2</sub>S ratio of the vent fluid [e.g., Baker and Massoth, 1987; Mottl and McConachy, 1990; Rudnicki and Elderfield, 1993; Field and Sherrell, 2000]. Particulates may subsequently dissolve, settle out of the plume, or remain suspended dependent on their composition and size. Elements with a high solubility in seawater (e.g., the alkalis) will stay almost entirely in solution throughout mixing within the plume and their flux into the ocean can be estimated accurately using the high-temperature hydrothermal flux. In contrast, elements that have a low solubility in seawater compared to vent fluids (e.g., chalcophile elements) are expected to rapidly precipitate forming particulates.

The formation and fate of particles in a hydrothermal plume depend on numerous factors including (i) the high-temperature hydrothermal fluid composition; (ii) the flux of both high-temperature and diffuse fluid; (iii) the chemical and biological processes that transfer elements into and out of particulates; and (iv) the physical oceanographic conditions that control transport of the plume. Understanding such complex inter-related systems requires an integrated approach that is best achieved in an area of intense long-term study for which different kinds of data exist. The Endeavour segment of the Juan de Fuca ridge provides such a location having been studied in detail for over three decades [e.g., Kelley et al., 2012]. There are five major high-temperature vent fields along the Endeavour segment and several other smaller fields along with numerous diffuse flow sites [e.g., Kelley et al., 2012]. The three southern fields (Mothra, Main Endeavour, and High Rise) are larger and better studied than the northern two (Salty Dawg and Sasquatch; Figure 1) with 98 active sites in the southern three fields compared to just 20 in the northern two fields [Jamieson et al., 2014]. Recently Ocean Networks Canada (ONC; <http://www.oceannetworks.ca/>) has installed power and internet to instruments in the southern portion of the Endeavour field allowing real time observations to be made. Additionally, annual maintenance cruises provide the opportunity to collect discrete samples and undertake oceanographic surveys.

Here we use the results of a new along and across axis tow-yo survey of the temperature and light attenuation anomaly in the water column, along with current meter data recording the flow field in the neutrally buoyant plume, to better understand the neutrally buoyant plume. We also report the composition of

sediments collected in a near-vent sediment trap and in sediment cores collected from a range of distances from the vents (up to  $\sim 3$  km). Despite extensive study of the Endeavour hydrothermal systems, very little comparable data have been collected [Dymond and Roth, 1988; Hrischeva and Scott, 2007]. The oceanographic data suggest that  $\sim 50\%$  of the plume temperature anomaly comes from particulate poor hydrothermal fluids. Sediment trap and sediment core sample compositions and mass accumulation rates indicate that the hydrothermal sediment composition changes substantially with distance from the vents but only a few percent of even the most insoluble elements are deposited within 1.5 km of the major vent fields.

### 1.1. Sample Locations and Sample Preparation Protocols

Sediment push cores were collected opportunistically during ONC maintenance cruises in 2012–2014 and 2016 (Figure 1). Sediments are generally thin along the axial valley and samples were collected in small-scale topographic lows where sediment has ponded (e.g., between pillows). Cores were stored in a freezer or cold room prior to preparation for analysis. Longer cores were subsectioned, generally into  $\sim 5$  cm intervals (supporting information Table 1), and then the sediment was dried at  $\sim 40^\circ\text{C}$  (without washing to avoid loss of easily dissolved or very fine material). Some cores contained centimeter-scale basalt fragments and these were picked out of the sediment. Fine-grained basaltic material, including fragmental material from explosive eruptions (supporting information Figure S1), was not separated from the cores. Dry core material was crushed in an agate planetary mill to produce a fine powder for geochemical analysis.

A sediment trap was deployed in the Main Endeavour field during the ONC maintenance cruise in 2014, with an 18 day sampling interval, and recovered in 2015. It was located  $\sim 40$  m south of the most active vent area that contains Grotto but north of the less active area that contains Bastille. Before deployment sediment trap bottles were washed and then filled with 5 M NaCl brine providing a dense solution to prevent loss of material from the bottles and spiked with formalin. Only the first 15 bottles (of 21) collected any significant sediment (supporting information Table S2) suggesting that the trap became clogged after this. The sediment was separated from the solution that they were collected in by filtering with a cleaned 1 mm Nitex mesh to remove “swimmers” and then collecting the sediment using a  $0.22\ \mu\text{m}$  Sarstedt Filtropur filter. The sediment was washed multiple times with deionized (DI) water and then the material that collected on the filter was back-washed into clean 500 mL glass vials and allowed to dry on a warm ( $\sim 40^\circ\text{C}$ ) hotplate in a laminar flow hood. All sample preparation took place in a class 100 clean room. After weighing (supporting information Table S2), samples were examined under a binocular microscope and then the majority of each sample was crushed by hand using an agate mortar and pestle to produce a homogeneous powder for analysis. A small amount of uncrushed material was preserved as an archive.

### 1.2. Analytical Methods

The major element compositions of the sediment core samples were analyzed by XRF, and C and S concentrations by LECO, at Acme Labs in Vancouver. The trace element compositions of all samples, and the major element compositions of the sediment trap samples (due to sample volume limitations), were analyzed using a Thermo X-series ICP-MS at the University of Victoria. Total carbon ( $C_{\text{total}}$ ), N, and S contents of sediment trap samples were measured using an elemental analyzer at the University of British Columbia. Their inorganic carbon ( $C_{\text{inorg}}$ ) contents were measured using a  $\text{CO}_2$  coulometer in the same lab with the organic C content ( $C_{\text{org}}$ ) calculated by difference.

Powdered samples were dissolved in Teflon vials for ICP-MS analysis using a modified HF,  $\text{HNO}_3$  dissolution procedure in which a small amount of oxalic acid was added to the second  $\text{HNO}_3$  step. Additionally, for some samples, an additional dissolution step using  $\text{H}_2\text{O}_2$  was added in an attempt to get refractory materials into solution. The final solution was diluted in 2%  $\text{HNO}_3$  to a sample mass ratio of between  $\sim 3000$  and  $\sim 12,000$  for analysis.

The standards BIR-1, BCR-2, DN-C, DR-N, IF-G, LKSD-2, IAEA-405, and SY-4 were used for calibration. Because these standards do not extend to as high concentrations as the samples, for some elements, a solution spiked with Mn, Cu, Zn, Ag, Sb, Ba, and Pb was prepared and added to splits of some of the standards. The spike was added at concentrations that led to a series of standards with concentrations similar to those of the unknowns allowing the linearity of the calibration curve from the low concentration standards up to the high concentration unknowns (for these elements) to be checked. In each case, the calibration curves

using the rock standards and using the spiked standards were very similar and the latter were used for calibrating the elements listed above. Primary drift was monitored using In, added on line, as the internal standard. Secondary drift was corrected for by running a solution of similar concentration to the unknowns (made by mixing aliquots of several unknowns) after every seven analyses. A second-order polynomial was fit through the In normalized count rates for this solution and used to drift correct the other solutions. A blank correction was performed using total procedural blanks although this was negligible for all elements except P.

Comparison of the Ba contents determined by XRF and ICP-MS shows that although in most samples these are similar, in some Ba-rich samples, the latter are much lower. These Ba-rich samples all come from <350 m from major vents. Because of the very low solubility of barite, the main source of Ba in these samples, this suggests a problem with the dissolution, or reprecipitation, of barite during preparation of samples for ICP-MS analysis. Strontium is concentrated in barite but the Sr content of these samples is not systematically lower in the ICP-MS data suggesting either that Sr was leached from barite or, more likely, that barite dissolved and then reprecipitated. To ensure that the sediment trap samples did not suffer from barite precipitation they were diluted immediately prior to analysis and their Ba contents were remeasured at the end of the analytical run and were found to be identical to at the start of the run. For the sediment core samples, the Ba contents from XRF analysis is used throughout. The Pb-isotopic compositions of three sediment trap samples and 12 sediment core samples were determined at the University of British Columbia following methods described in *Weis et al.* [2006].

Volcanic glass fragments separated from some sediment cores were gently crushed and visually alteration-free portions were picked under a binocular microscope then mounted in epoxy and polished for analysis. Glass major element compositions were determined by electron microprobe at the University of British Columbia using a Cameca SX-50 with a 20  $\mu\text{m}$  beam diameter, 20 nA beam current, and 20 kV accelerating voltage. Trace element compositions were determined using a New Wave 213 nm laser linked to the same ICP-MS used for solution analysis. A 90  $\mu\text{m}$  spot and 10 Hz repetition rate were used and the ablated material was transported from the laser cell to the ICP-MS in He. Calibration used Ca as the internal standard (as determined by electron microprobe) and NIST 612 as the single calibration standard.

## 2. Results

### 2.1. Oceanographic Data

A tow-yo survey both along and across axis (Figure 1) was performed during the 2015 ONC maintenance cruise using a Seabird 911 CTD rosette with a WET labs CSTAR transmissometer. The neutrally buoyant plume is clearly observed in both the temperature and transmissivity anomalies in the water column (Figure 2). It extends up to  $\sim 1900$  m depth in the water column as has previously been observed in this area [*Baker and Massoth, 1987; Thomson et al., 1992; Kellogg and McDuff, 2010*]. The plume is most clearly observed along the axis and over the western flank with no obvious signal over the eastern flank (Figure 2). The transport of material along axis and over the western flank is consistent with previous studies [e.g., *Baker and Massoth, 1987; Feely et al., 1992*] and water column mooring current meter data (see below).

In order to determine the average dilution factor of the vent fluid in the neutrally buoyant plume, we calculated the average temperature anomaly within this layer. The top of the neutrally buoyant plume is assumed to be at 1900 m depth but the base of the plume is more difficult to define; to a first approximation, we assume it is 200 m thick putting most of the neutrally buoyant plume above the edges of the axial valley meaning that it can be advected off axis. Averaging all along axis, temperature measurements (Figure 2) in the 1900–2100 m depth range gives an average temperature anomaly of  $0.043^\circ\text{C}$ , similar to previous measurements [e.g., *Baker and Massoth, 1987; Thomson et al., 1992; Kellogg and McDuff, 2010*]. Based on published data, black smoker vent fluid temperatures at Endeavour are between  $\sim 300$  and  $380^\circ\text{C}$  [*Butterfield et al., 1994; Seyfried et al., 2003; Bao et al., 2008; Lin et al., 2016; Germanovich et al., 2015*]. A single vent in the Main Endeavour field has been monitored through the ONC cabled observatory and has maintained a temperature of  $333 \pm 2^\circ\text{C}$  ( $1\sigma$ ) over a 6 year interval (September 2010 to July 2016; data at <http://dmas.uvic.ca/DataSearch>) consistent with the published vent fluid temperatures. Assuming an average vent fluid temperature of  $350^\circ\text{C}$ , and a water column temperature anomaly of  $0.043^\circ\text{C}$ , gives a dilution factor of 8000. However, much of the venting fluid may be much lower temperature diffuse flow generated in the subsurface.



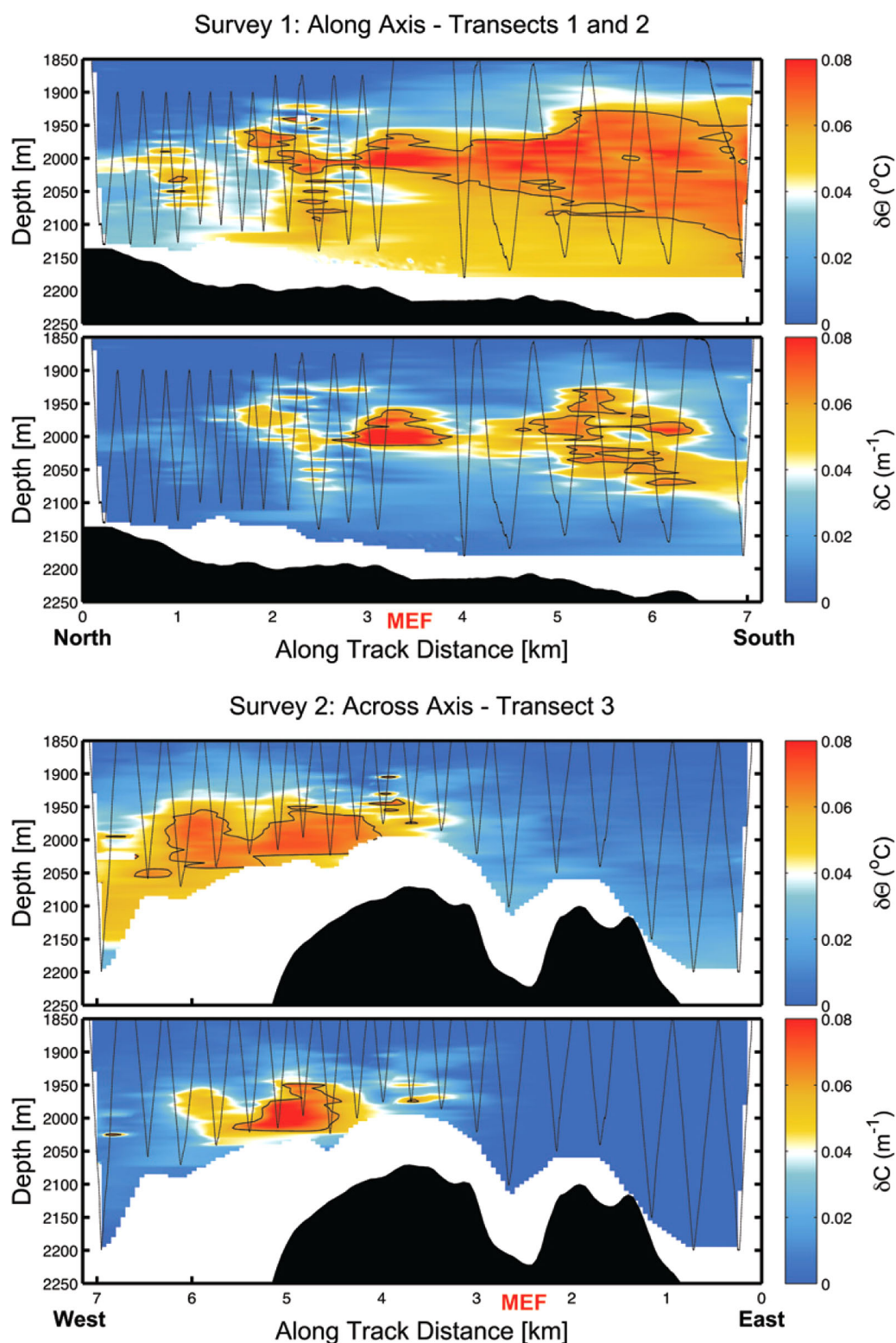


**Figure 2.** (top) Along and (bottom) across axis tow-yo survey results for potential temperature ( $\delta\Theta$ ) and transmissivity ( $\delta C$ ) anomalies. See Figure 1 for survey locations.

The relationship between the temperature and light attenuation anomalies potentially provides information about the proportion of heat add by diffuse flow. High-temperature (black smoker) fluid leads to the addition of both heat and particulates to the water column whereas diffuse flow adds heat but not particulates

(the elements that would form particulates are deposited in the subsurface) [e.g., *Edmond et al.*, 1979]. This difference can explain why the ratio of the light attenuation anomaly to potential temperature anomaly in hydrothermal plumes can show a clear maximum (in this case  $\sim 1.25 \text{ m}^{-1} \text{ }^{\circ}\text{C}^{-1}$ ) but with much of the plume having an excess of potential temperature with respect to light attenuation (Figure 3a) [cf., *Baker and Massoth*, 1987]. This excess in potential temperature relative to particulates can either come from diffuse flow adding heat, or particle sedimentation or agglomeration decreasing the attenuation anomaly. Sediment geochemistry (see below) indicates only a very small fraction of the particulate matter sediments out within a few km of the axis and hence the former model is more plausible. To quantify the excess potential temperature ( $PT_{XS}$ ) relative to particulates we simply subtract 0.8 times the light attenuation anomaly from the measured potential temperature. Along the axis,  $PT_{XS}$  is much more evenly distributed both vertically in the water column and with distance along axis compared to the potential temperature and light attenuation anomalies (Figure 3). This is consistent with this heat being supplied by broadly distributed diffuse flow. The average  $PT_{XS}$  calculated the same way as the average potential temperature anomaly is  $0.025^{\circ}\text{C}$ , roughly half of the average potential temperature anomaly; while this is a very rough approximation of the temperature anomaly derived from diffuse flow it is consistent with some previous studies [*Chin et al.*, 1994; *Veirs et al.*, 2006]. This contrasts with other estimates that diffuse flow carries  $\sim 90\%$  of the heat flux [e.g., *Schultz et al.*, 1992; *Rona and Trivett*, 1992] and may require upward estimates of the hydrothermal fluxes of elements that are concentrated in high but not low-temperature fluids (e.g., chalcophiles); i.e., a smaller fraction of these elements may be deposited during subsurface mixing and cooling than has previously been suggested. There is also a significant  $PT_{XS}$  anomaly off axis on the west flank (Figure 3c). Whether this reflects heat addition by off-axis discharge of diffuse fluids, or particle sedimentation or agglomeration decreasing the attenuation anomaly, is unclear and awaits future study.

There are four water column moorings in the Endeavour area, two north of High Rise and two north of Mothra (Figure 1) with Nortek Aquadopps single point acoustic current meters deployed at 125 m, and in some cases 200 m, above the bottom. Progressive vector displacements for the currents recorded by the instruments in the south over 16 weeks (23 May to 12 September 2016; data at <http://dmass.uvic.ca/Data-Search>) indicate flow at the plume height toward the SW (supporting information Figure S2), as has been suggested previously [*Baker and Massoth*, 1987; *Feely et al.*, 1992]. This current direction is consistent with the observation of a water column temperature and light scattering anomaly over the west but not east flank (Figure 2). Progressive vector displacements for the currents recorded at the northern moorings are toward the S and SE at the two moorings, respectively. Generally, southward flow may reflect the drawing of water into the axial valley to replace water carried upward by entrainment of water into hydrothermal plumes [*Thomson et al.*, 2003]; the origin of the eastward vector of flow at the NW mooring is unclear. The current meter data show that the average flow velocity varies with height in the water column and with location in the range  $\sim 0.7\text{--}3 \text{ cm s}^{-1}$  similar to previous observations ( $0.4\text{--}4 \text{ cm s}^{-1}$ ) [*Baker and Massoth*, 1987; *Thomson et al.*, 2005]. Because of the heterogeneity in the speed and direction of flow, it is not possible to accurately determine the heat flux that is being transported out of the axial valley from these data.

## 2.2. Sediment Trap and Sediment Core Compositions

The aim of this study is to investigate the long-term fluxes associated with ridge axis hydrothermal systems and thus we do not discuss the details of the temporal variation in the sediment trap samples here. That said, it is notable that the third and fourth samples collected contain roughly 6 times more material than the others and these are compositionally distinct in a number of ways including having the highest  $C_{org}/N$  and being  $\sim 10$ -fold enriched in Na. Leaching with deionized water demonstrated that these samples contain  $>50\%$  NaCl suggesting that the brine in the sediment trap bottle saturated in NaCl contaminating these samples. These samples are excluded in calculating the average sediment flux and composition of the sediment trap material.

The average sedimentation rate based on the sediment trap samples was  $21 \pm 9 \text{ g yr}^{-1} \text{ m}^{-2}$  which is within uncertainty the same as the sedimentation rate of  $25 \pm 6 \text{ g yr}^{-1} \text{ m}^{-2}$  observed by *Dymond and Roth* [1988] for a sediment trap deployed beneath the neutrally buoyant plume near the High Rise vent field. This sedimentation rate is, however, much lower than the sedimentation rate observed by *Dymond and Roth* [1988] for a sediment trap deployed within the buoyant plume at the Main Endeavour field of  $275 \text{ g yr}^{-1} \text{ m}^{-2}$ . The large mass flux they reported within the buoyant plume is  $\sim 80 \text{ wt } \% \text{ S, Fe, and Ca}$  suggesting abundant Fe-sulfide and anhydrite sedimentation from the buoyant plume. Extensive precipitation of Fe-sulfides close to

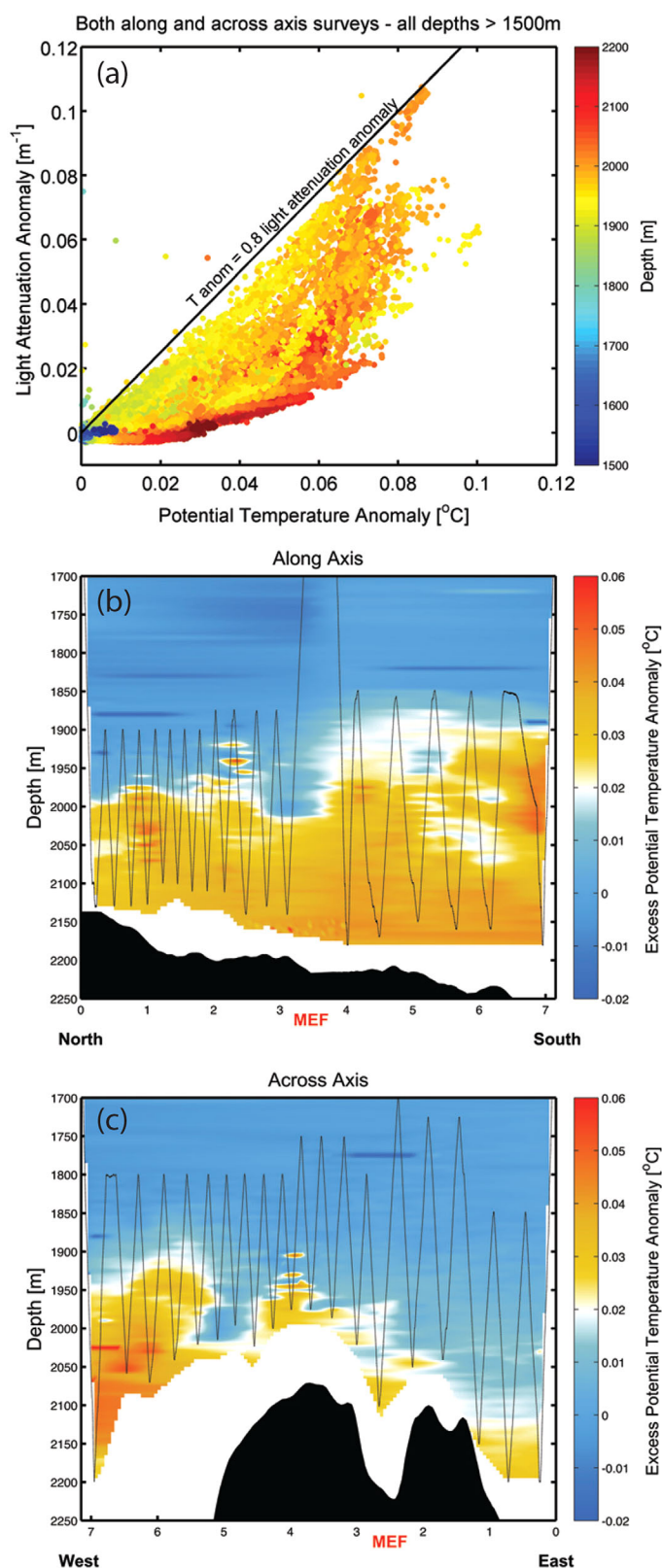


**Figure 3.** (a) Crossplot of light attenuation anomaly and potential temperature anomaly color coded by measurement depth. There is a clear maximum in light attenuation for any given temperature anomaly but much of the water column has excess potential temperature relative to light attenuation. (b) Along and (c) across axis profiles of the excess potential temperature anomaly relative to the measure light attenuation; see text for details.



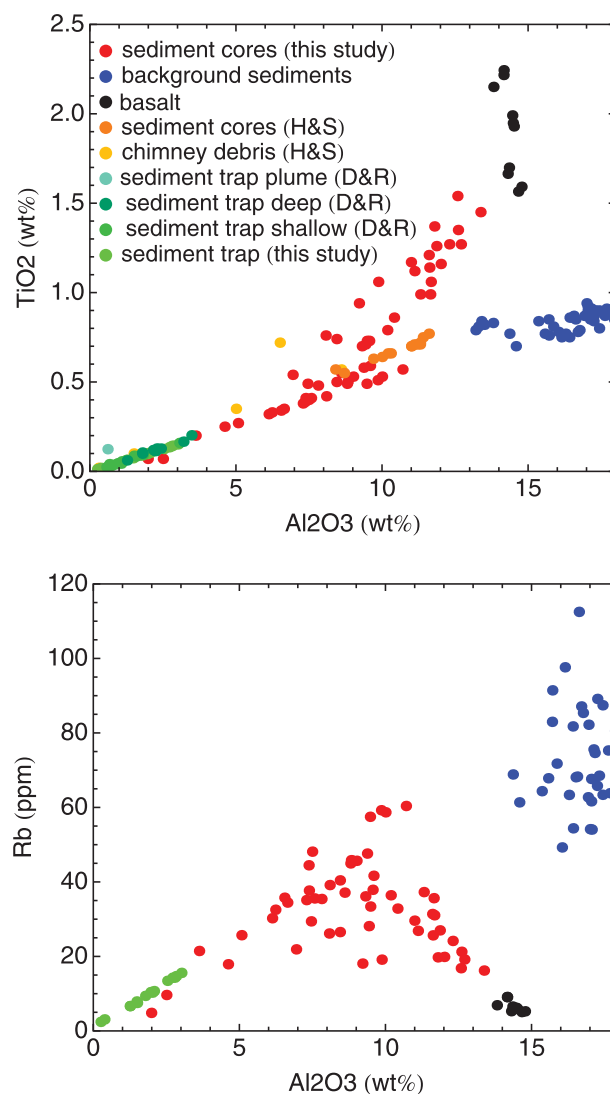


**Figure 4.** Comparison of the lithophile element abundances in the sediment trap and sediment core samples with the composition of basalt fragments in the cores and background sediments [Carpentier *et al.*, 2013; Hrischeva and Scott, 2007]. Sediment trap samples have low lithophile element abundances and show no evidence of any basalt fragments. Sediment core samples can be explained as mixtures of a hydrothermal component similar to that in the sediment trap samples (i.e., close to the origin in these plots), background sediment and, in some cases, basalt fragments. DR: Dymond and Roth [1988]; HS: Hrischeva and Scott [2007].

the composition of basalt fragments separated from the cores (Figure 4). These elements are used below to quantify the mass fractions of basalt and terrigenous material in the sediment cores. However, the bulk concentrations of some elements in the sediment cores are described first to introduce the data.

The composition of the sediments changes systematically with distance from the major vent fields (Figure 5) reflecting changes in the proportion, and composition, of the hydrothermal contribution to the sediments. This observation suggests that the locations of the major vent fields have not changed substantially over the duration of the deposition of these sediments ( $\sim 2000$  years based on  $^{14}\text{C}$  dating of samples from the axial valley) [Clague *et al.*, 2014]. This is consistent with ages of the chimney structures that indicate that venting began at High Rise and Main Endeavour  $\geq 850$  and 2300 years ago, respectively [Jamieson *et al.*, 2013]. Additionally this suggests that venting from the numerous inactive chimneys scattered along the axial valley (Figure 1) did not contribute substantially to the hydrothermal sediment compositions.

the vents is expected considering the high molar  $\text{H}_2\text{S}/\text{Fe}$  ( $\gg 1$ ) of these vent fluids [Butterfield *et al.*, 1994; Seyfried *et al.*, 2003].

Non-hydrothermal sediment makes up a component of both the sediment core and sediment trap samples and basalt fragments (both from explosive volcanism and underlying lava flows) make up a portion of some of the sediment core samples (e.g., supporting information Figure S1). Nonhydrothermal sediment includes both terrigenous material and a biogenic component (both organic matter and shell fragments). The biogenic component is difficult to assign an exact composition to due to variable diagenetic loss but the terrigenous component can be approximated by the composition of sediments from the Cascadia basin [Carpentier *et al.*, 2013] and Nootka fault [Hrischeva and Scott, 2007]. The average composition of basalt fragments picked from the cores provides an estimate of the average composition of the basalt component in the sediments. Geochemically, the basaltic and terrigenous sediment components can be identified in the covariation of elements such as Li, Al, K, Ti, and Rb in the bulk sediments because the hydrothermal and biogenic components provide negligible amounts of these (Figure 4). Sediment trap samples lie on a mixing line between a hydrothermal component (virtual zero concentration of all of these elements) and detrital sediments from the Cascadia basin and Nootka fault. The maximum contribution of terrigenous material to the sediment trap samples is  $\sim 25\%$ . Some sediment core samples lie along the same mixing line with others offset from this toward

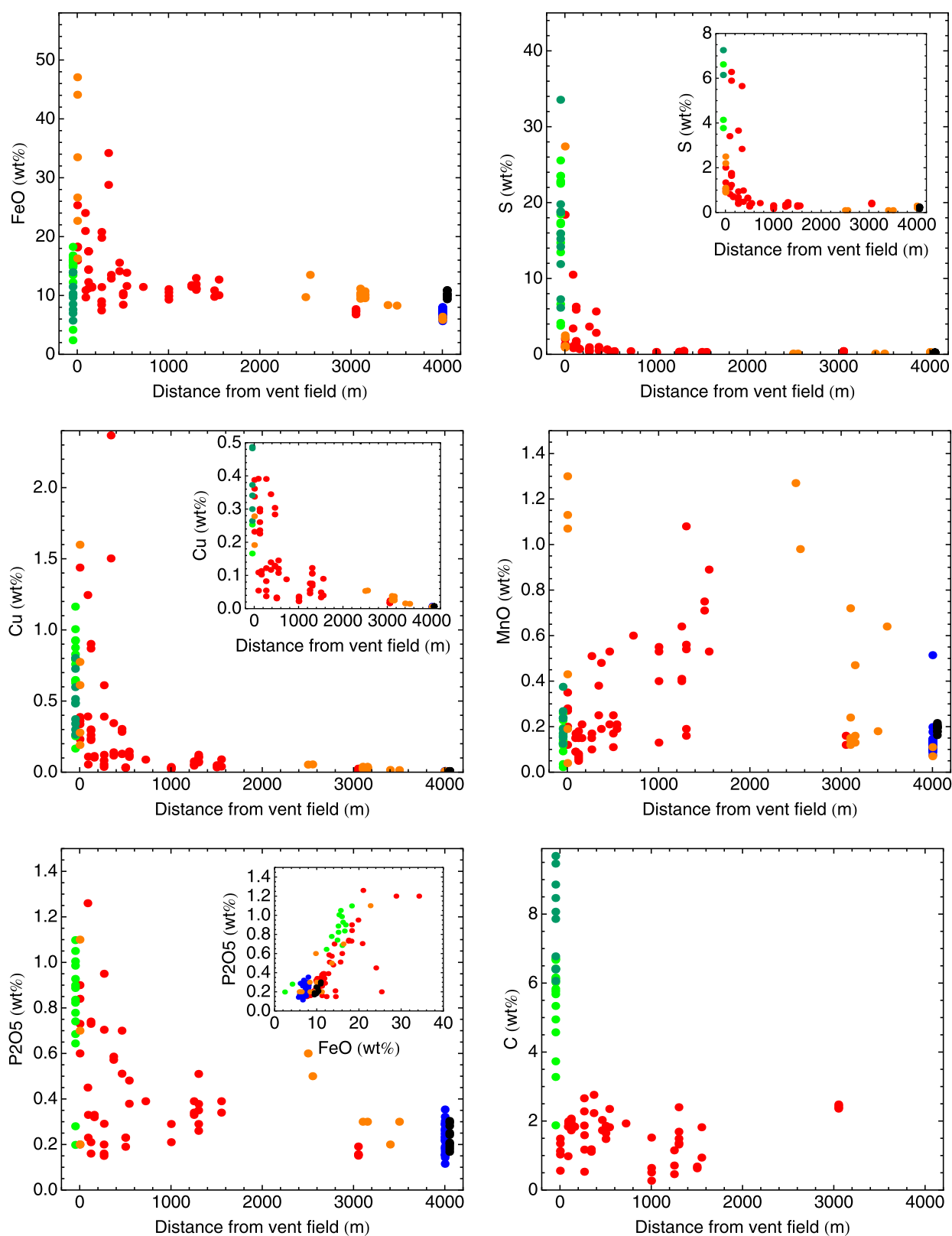


**Figure 5.** Variation in sediment compositions with distance from the major vent fields with sediment trap samples plotted at a negative distance for clarity. Symbols as in Figure 4. Background sediments (4000 m) and basalts (4050 m) are plotted at an arbitrary distance.

The sediment trap samples from this study contain up to 18 wt % FeO, 1.2 wt % Cu, and 26 wt % S, similar to the sediment trap samples from near the High Rise field reported by *Dymond and Roth* [1988], indicating a large hydrothermal component (Figure 5). Iron, Cu, and S concentrations are also high or extremely high in sediments close to the vent fields, with concentration exceeding those in the sediment traps in a few samples. Those near-vent sediment core samples that have higher Fe and Cu contents than the sediment trap samples may contain degraded chimney material as well as plume fallout. The Cu and S contents of the sediments decrease rapidly with distance from the vents suggesting rapid accumulation of sulfide particles from the buoyant plume. Chalcophile trace elements (As, Ag, Cd, Sb, and Pb) show broadly similar distributions to Fe, Cu, and S. The Mn content of the sediment cores generally increases with distance from the vents (Figure 5) consistent with the well-known slow oxidation kinetics for Mn within hydrothermal plumes [e.g., *Cowen et al.*, 1990; *Lavelle et al.*, 1992]. However, sediment cores collected >500 m from the vents generally show a decrease in Mn with depth in the core suggesting diagenetic mobilization redistributing Mn upward within these sediments [e.g., *Lavelle et al.*, 1992]. This complicates interpretation of the spatial distribution of Mn in the sediments. Phosphorous is highly enriched in the sediment trap samples and in some sediments close to the vent fields then drops to near background levels (Figure 5). Elevated P in the near-vent sediments (Figure 5) and a broadly coincident linear correlation between Fe and P in the sediment core and sediment trap samples suggest that P is efficiently scavenged from seawater in the buoyant plume as has been suggested previously [e.g., *Feely et al.*, 1991]. The  $C_{\text{total}}$  content of the sediment trap samples is much higher than the sediment core samples and there is no change in the  $C_{\text{total}}$  content of the sediment cores with distance from the vents (Figure 5). This distribution suggests that diagenetic processes lead to substantial C loss from the sediments soon after their deposition. This may reflect both dissolution of  $\text{CaCO}_3$  (e.g., pteropods, which have aragonite shells, were observed in sediment trap samples) and degradation of  $C_{\text{org}}$ .

### 3. Discussion

The compositions of the sediments around the Endeavour field are mixtures of multiple components including at least (i) a hydrothermal component; (ii) background terrigenous material and biogenic debris (organic matter and shell fragments); (iii) basalt fragments; and, for the sediment core samples; and (iv) salt precipitated from interstitial water. We use a linear mixing model to estimate the mass fraction and composition of the hydrothermal component in each sample. We then investigate the variation in the mass and composition of the hydrothermal component with distance from the high-temperature vent sites and discuss the causes of the spatial variations in composition. Finally, we construct a simple mass balance model that constrains the fraction of an element in the high-temperature fluid that is deposited within 1.5 km of the vents and consider the role of scavenging from the overlying water column.

#### 3.1. Extracting the Hydrothermal Component of the Sediment Core Compositions

The composition of the basalt and background sediment components are not expected to vary systematically with distance from the vents, unlike the hydrothermal component, meaning that to a first approximation the proportion of these can be calculated from the lithophile element abundance in the sediments. That said, because the biogenic component of the background sediment will undergo diagenetic mass loss its composition in the sediment trap and sediment core samples is expected to differ somewhat.

The concentrations of elements such as Li, Al, K, Ti, and Rb in the sediments are controlled by the abundance of basalt fragments and background sediment (Figure 4). These elements all behave very similarly, as “lithophile” elements, in the sediment trap data (which are basalt free) with the maximum relative standard deviation ( $\% \text{RSD} = 100\sigma/\text{mean}$ ) in the ratios of these elements to one another being <7%. Likewise, the ratios of these elements in the average sediments from the Cascadia basin [*Carpentier et al.*, 2013], after filtering these data to exclude carbonate-rich samples (>25 wt % CaO) and Si-rich samples (>60 wt %  $\text{SiO}_2$ ), are within a factor of 1.2 of those from the sediment traps. In contrast, the ratios of these elements to one another in the basalts are very different than in the sediments (e.g., Figure 4). Based on these observations, this group of elements are used to determine the mass fractions of basalt and background sediment in the samples.

The mass fractions of basalt, background sediment and NaCl in the samples are calculated by assuming that all the Na, Ti, Al, Li, K, and Rb in the samples comes from one of these components and solving the

linear mass balance problem under the constraints that mass fractions are  $\geq 0$  and the sum of these components is  $\leq 1$ . All concentrations were normalized to the average sediment composition and the misfit was calculated as the sum of the difference between the measured and modeled normalized concentrations of these elements. The average basalt composition is taken from the data reported here (supporting information Table 3) and the average nonhydrothermal sediment is derived from the data for sediments from the Cascadia basin after filtering out high Ca and Si samples as described above [Carpentier *et al.*, 2013]. The  $\text{Al}_2\text{O}_3/\text{TiO}_2$  of the average background sediment determined this way is virtually identical of that of material collected in sediment traps above the neutrally buoyant plume at the Endeavour ridge (19.9 versus 20.4) [Carpentier *et al.*, 2014; Dymond and Roth, 1988].

For the sediment trap samples, which have not undergone the same diagenetic loss of biogenic components as the background sediments, we calculate the mass fraction of the biogenic component as follows. The concentrations of  $\text{C}_{\text{org}}$  and N are summed to give a mass of organic matter. The concentration of  $\text{C}_{\text{inorg}}$  is converted into a concentration of  $\text{CaCO}_3$  (by multiplying by 8.33) and the concentration of biogenic silica is calculated from the concentration of  $\text{CaCO}_3$  using the linear correlation between these in the sediment trap samples reported by Dymond and Roth [1988] (biogenic silica =  $0.68\text{CaCO}_3$ ).

Using this mass balance approach, the sediment trap samples contain an average of  $14 \pm 4\%$  background sediment and  $0\%$  basalt component. Using the total sediment accumulation rate from the sediment trap data ( $21 \pm 9 \text{ g yr}^{-1} \text{ m}^{-2}$ ), this gives a background sediment accumulation rate of  $2.9 \pm 1.3 \text{ g yr}^{-1} \text{ m}^{-2}$ . Applying the same approach to the push core samples shows that together the basalt and background sediment components make up 12–90% of the samples, with cores collected  $>500 \text{ m}$  from the vent fields being comprised of  $>50\%$  background sediment and basalt. Overall, basalt fragments comprise  $20 \pm 23\%$  of the push core samples and background sediment  $40 \pm 14\%$ . For the sediment trap samples, the mass fraction of the hydrothermal component is calculated as 1 minus the mass fractions of background sediment, NaCl, organic matter, calcite, and biogenic silica and makes up 56–70% of the sediment. For the sediment core samples, the mass fraction of the hydrothermal component is calculated as 1 minus the mass fractions of basalt, background sediment, and NaCl.

The mass accumulation rate of hydrothermal sediment ( $\text{MAR}_h$ ) in the samples can be estimated using the calculated ratio of the mass fraction ( $M$ ) of hydrothermal sediment ( $h$ ) to the mass fraction of background sediment ( $bs$ ) and the measured rate of background sediment accumulation from the sediment trap:

$$\text{MAR}_h (\text{g yr}^{-1} \text{ m}^{-2}) = 2.9 M_h / M_{bs} \quad (1)$$

This approach is valid if we assume that the background sediment accumulates uniformly at the rate determined from the sediment trap studies. This assumption appears reasonable given that the accumulation rate of Ti (a lithogenic element) is the same in the sediment trap samples described here as in the sediment traps deployed at depths between 1200 and 2100 m near the High Rise vent field by Dymond and Roth [1988] in 1984 (both gave  $1.3 \pm 0.6 \mu\text{g cm}^{-2} \text{ yr}^{-1}$ ). The sediment trap data suggest a hydrothermal sediment accumulation rate of  $13 \pm 6 \text{ g m}^{-2} \text{ yr}^{-1}$ . The mass accumulation rate of hydrothermal sediment calculated for the sediment core samples decrease systematically from similar to that determined from the sediment trap near the vents to between 1 and  $2 \text{ g m}^{-2} \text{ yr}^{-1}$   $> 1000 \text{ m}$  from the vents (Figure 6).

### 3.2. Spatial Variation in the Composition of the Hydrothermal Component

The composition of the hydrothermal component in the samples can be estimated by removing the basalt ( $b$ ), background sediment and salt ( $s$ ) and, for the sediment traps samples, biogenic ( $bio$ ) components from the bulk composition:

$$X_h = \frac{X_{\text{bulk}} - M_b X_{bs} - M_{bg} X_{bg} - M_s X_s - M_{bio} X_{bio}}{1 - M_b - M_{bg} - M_s - M_{bio}} \quad (2)$$

where  $X$  = element concentration. While this approach has significant uncertainties associated with it, the results are still useful for understanding how the composition of the biogenic component changes with distance from the vents.

The composition of the hydrothermal component of the sediments, including the sediment trap samples, is illustrated in Figure 7. Element ratios to Fe are shown to facilitate comparison between the sediment compositions and chimney and vent fluid compositions. The sediment trap and near-vent sediment core

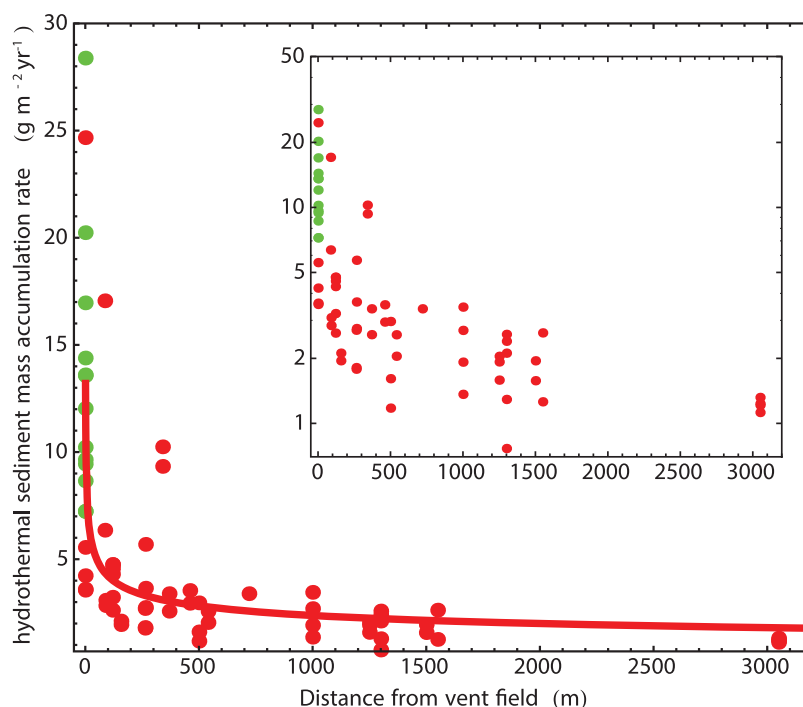


**Figure 6.** Calculated mass accumulation rate of the hydrothermal component of the sediments with variation in distance from the major vent fields. Sediment trap samples in green (plotted at a negative distance for clarity) and sediment core samples in red. A power law fit through the data is shown. The inset shows the same on a log scale.

samples have similar element-to-Fe ratios for most elements. This suggests both that the composition of the hydrothermal component has not varied substantially over time and that diagenetic processes do not massively modify the concentrations of these elements in vent proximal samples. Below we group elements with similar behavior and discuss the controls on their distribution in the hydrothermal component of the sediments.

### 3.2.1. Cd, Ag, Cu, Co, and Fe

Differing rates of metal accumulation into the sediments with distance away from the vents may reflect: (i) differing rates of metal-bearing particle formation and settling; (ii) differing rates of dissolution of metal-bearing particles that formed early in the life of the plume; and/or (iii) differing rates of scavenging of elements from the water column. The relative rates at which elements accumulate from the hydrothermal plume into the sediments can be determined using the change in the ratio of two elements with distance from the high-temperature vent fields. A decrease in an element ratio with increasing distance from the vent fields indicates that the numerator is accumulated into the sediments more rapidly than the denominator (assuming neither element is subsequently lost from the sediment). Using this approach, the data suggest that the relative order of accumulation is  $\text{Cd} > \text{Ag} > \text{Cu} > \text{Co} \sim \text{Fe}$  with substantial fractionation between these elements over the first  $\sim 500$  m from the high-temperature vent fields (Figure 7).

Comparing element-to-Fe ratios in chimney structures from the Endeavour segment [Hannington *et al.*, 2004; Kristall *et al.*, 2011] to that in the hydrothermal component of the sediment trap samples suggests a similar order of enrichment in the chimneys over the near-vent sediment ( $\text{Ag} > \text{Cd} > \text{Cu} > \text{Co} > \text{Fe}$ ; Figure 7). Vent fluid element-to-Fe ratios are generally lower than in the hydrothermal component of the near-vent sediments for Cd, Ag, and Cu but higher than in the distal sediments (Figure 7) consistent with earlier sedimentation of these elements than Fe from the plume. The Co/Fe of the vent fluids, chimneys, sediment trap samples and sediment core samples are all remarkably similar (Figure 7) suggesting that these elements behave very similarly throughout the Endeavour hydrothermal system.

The distribution of Cd, Ag, Cu, Co, and Fe in the sediments can be explained by the formation of metal sulfides in the hydrothermal plume (and chimneys) with the affinity for the sulfides being strongest for Cd and Ag, followed by Cu and then Co and Fe. The high  $\text{H}_2\text{S}/\text{Fe}$  of the Endeavour vent fluids means that sulfides



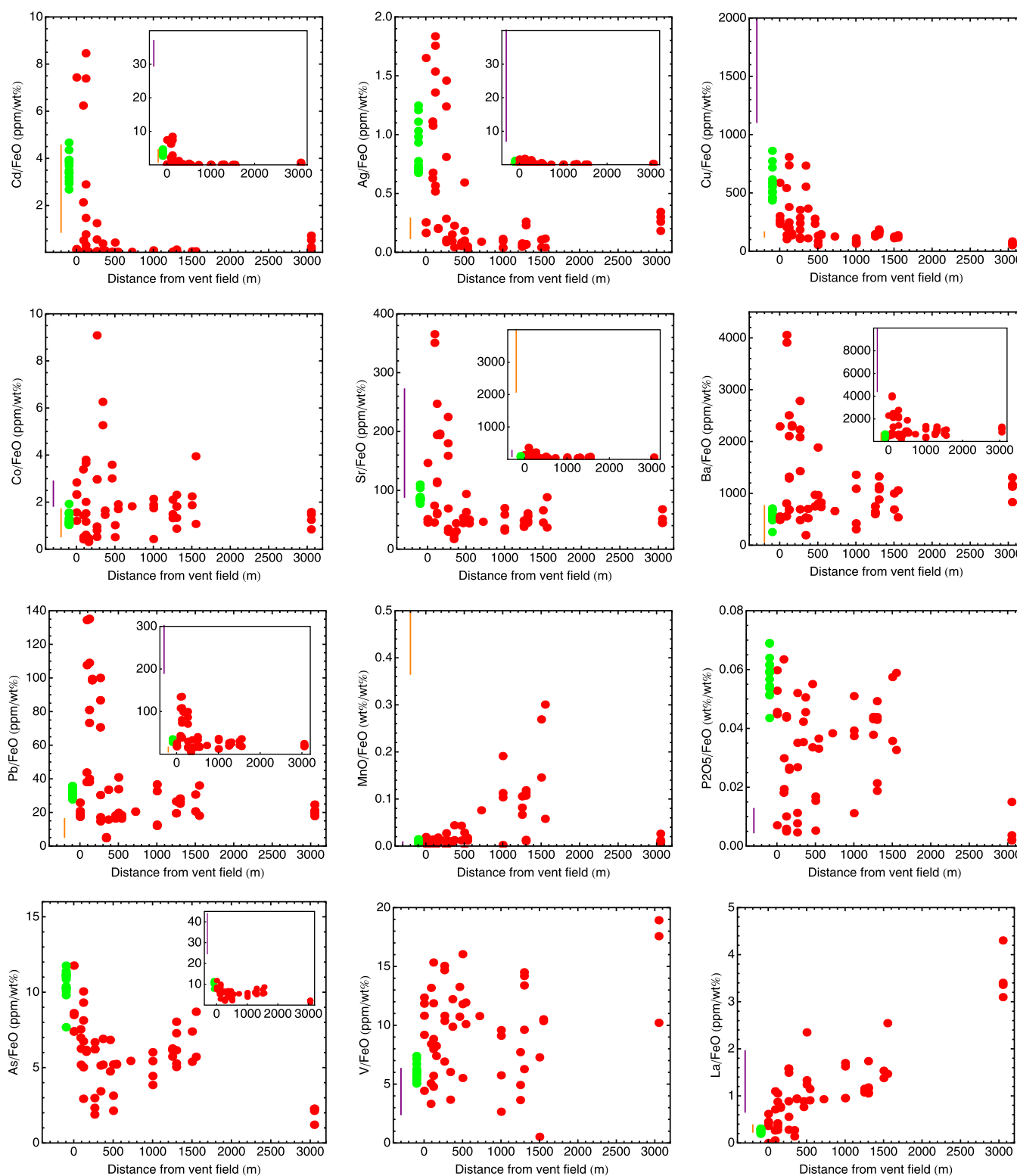


**Figure 7.** Calculated element/FeO ratio in the hydrothermal component of the sediments shown as a function of distance from the major vent fields. Sediment trap samples in green (plotted at a negative distance for clarity) and sediment core samples in red. Also shown are the average (and one standard deviation) of the compositions of hydrothermal chimneys (purple) [Hannington et al., 2004; Kristall et al., 2011] and vent fluids (orange) [Butterfield et al., 1994; Seyfried et al., 2003; Bao et al., 2008; Lin et al., 2016] from the Endeavour segment (also plotted at a negative distance for clarity).

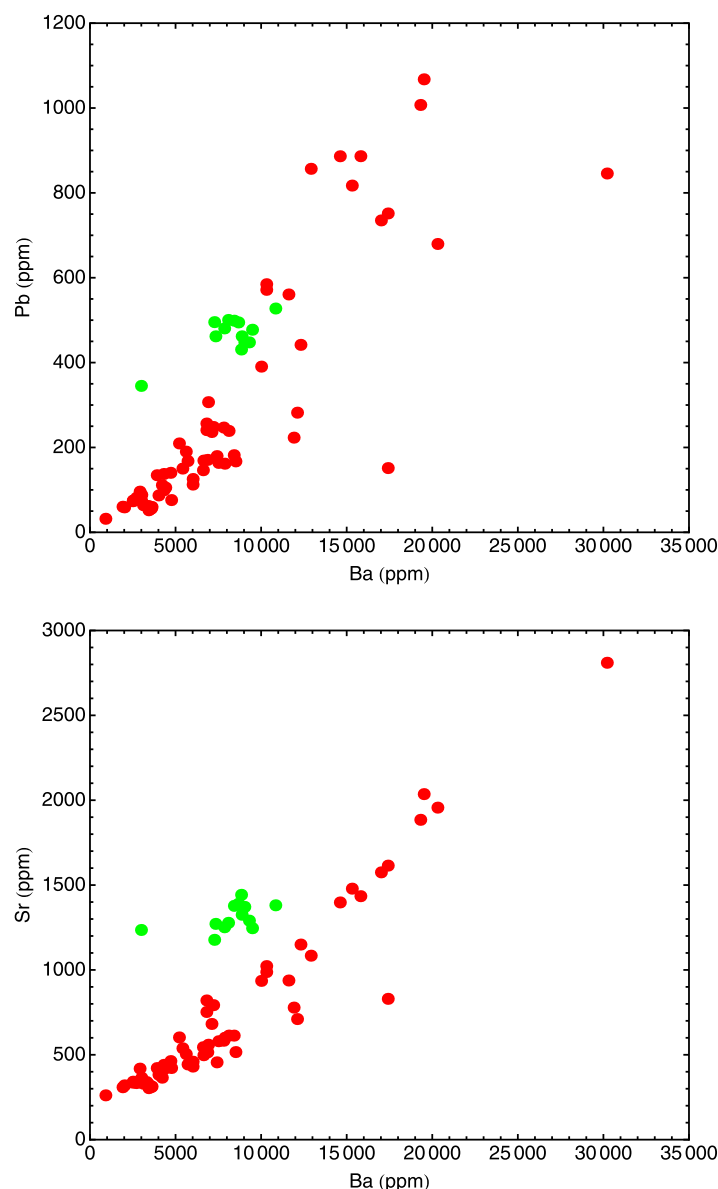


**Figure 8.** Crossplots of Ba against (a) Pb and (b) Sr for the sediment core (red) and sediment trap (green) samples. The correlation of these element abundances, and the almost identical Sr/Ba of the sediments and barite in hydrothermal chimneys from the Endeavour area [Jamieson *et al.*, 2016], suggests that these elements may all be controlled by the distribution of barite ( $\pm$  other sulfates) in the sediments. The somewhat higher Sr content of the sediment trap samples for a given Ba content probably reflects the existence of anhydrite in these samples. One sample from very close to a chimney is not shown as its very high Ba content would compress the scale substantially.

samples have somewhat higher Sr/Ba than the sediments collected in push cores or barite, possibly reflecting the existence of some Sr-rich anhydrite that will not be preserved in sediments deposited on the seafloor (Figure 8). Measured Pb concentrations in barite from hydrothermal chimneys at Endeavour are low ( $<10$  ppm) [Jamieson *et al.*, 2016] suggesting that barite precipitated with sulfides is Pb poor. However, angle-site ( $\text{PbSO}_4$ ) is isostructural with barite [e.g., Antao, 2012] and it is plausible barite precipitated from the hydrothermal plume is more enriched in Pb than barite precipitated within a chimney. Alternatively, it is possible that  $\text{PbSO}_4$  is directly precipitated from the plume.

The simplest explanation of the high Sr, Ba and Pb content of the sediments at intermediate distances from the vents is that these are incorporated into sulfates which are deposited a few 100 m from the vents.

will form rapidly in the buoyant plume as has been observed elsewhere [e.g., Mottl and McConachy, 1990]. This is consistent with the very high sulfide content of sediment collected using a sediment trap within the buoyant plume at the Main Endeavour field [Dymond and Roth, 1988]. The rapid drops in Cd/Fe, Ag/Fe, and Cu/Fe in the hydrothermal component of the sediments within 500 m of the vents shows that sulfide accumulation is concentrated close to the vents although it is shown below that most of these metals released into the water column are advected much further away.

### 3.2.2. Sr, Ba, and Pb

The ratios of Sr, Ba, and Pb to Fe in the hydrothermal component of the sediments is highest  $\sim 100$ –250 m from the vents and lower both closer to (including in the sediment trap), and further from, the vent fields (Figure 7). Relatively low near-vent Pb was also observed in a single sediment core from the EPR [German *et al.*, 1999]. The Ba, Sr, and Pb contents of the hydrothermal sediments correlate strongly (Figure 8) suggesting that the same or similar process(es) may be controlling the behavior of these elements. The Sr/Ba of the hydrothermal component of the sediment core samples (0.07) is within uncertainty the same as that of barite from hydrothermal chimneys along the Endeavour segment (0.06) [Jamieson *et al.*, 2016]. The sediment trap sam-

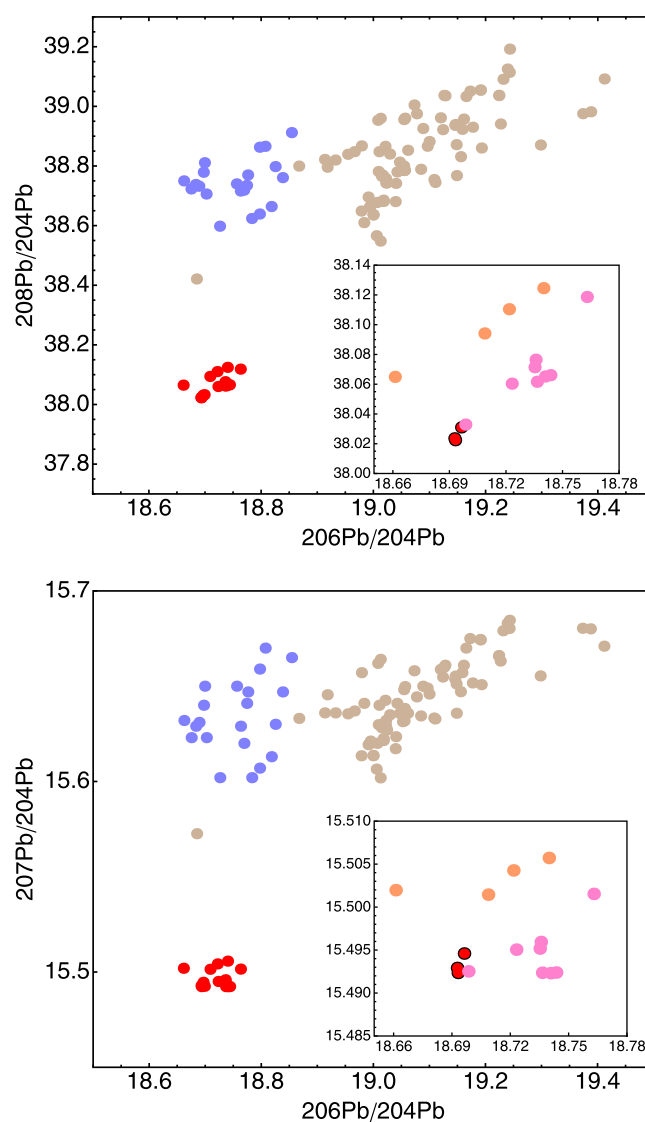


**Figure 9.** Pb-isotope crossplots comparing the composition (averages are shown as the large symbols) of hydrothermal chimney sulfides at Endeavour (black) which represent the hydrothermal end-member, with background sediments (brown) and Pacific seawater as determined from Mn nodules (blue) with the samples from this study (red). The insets zoom-in on the samples from this study showing that the sediment trap samples (red with black outline) have the highest hydrothermal component and samples <300 m from the vents (pink) are largely mixtures of hydrothermal and background sediment components. In contrast, samples from >1000 m from the major vent fields (orange) contain a larger amount of Pb scavenged from seawater. See text for discussion.

nodules from the Pacific [von Blanckenburg *et al.*, 1996]. These have similar  $^{206}\text{Pb}/^{204}\text{Pb}$  to hydrothermal sulfides, but much higher  $^{207}\text{Pb}/^{204}\text{Pb}$  and  $^{208}\text{Pb}/^{204}\text{Pb}$  (Figure 9).

The sediment trap samples and push core samples collected close to the vents have Pb-isotopic compositions most similar to the massive sulfides indicating a dominantly hydrothermal source of Pb. However, even these samples have more radiogenic Pb than the chimney sulfides indicating that they contain some seawater and background sediment Pb. Push core samples collected far from the vents (>1 km) have relatively higher  $^{207}\text{Pb}/^{204}\text{Pb}$  and  $^{208}\text{Pb}/^{204}\text{Pb}$  at a given  $^{206}\text{Pb}/^{204}\text{Pb}$  than samples collected closer to the vents (Figure 9 insets). This offset toward higher  $^{207}\text{Pb}/^{204}\text{Pb}$  and  $^{208}\text{Pb}/^{204}\text{Pb}$  at a given  $^{206}\text{Pb}/^{204}\text{Pb}$  suggests greater scavenging of seawater Pb with great transport distance away from the vents. Simple linear mixing models, using the average compositions of these three end-members, indicate that ~90%

Possible sources of sulfate include oxidation of hydrothermal  $\text{H}_2\text{S}$ , oxidizing sulfide minerals and seawater sulfate; the high dilution factors make the latter by far the dominant sulfate reservoir within the neutrally buoyant plume. The high  $\text{H}_2\text{S}/\text{Fe}$  of the vent fluid, and high Ba content of many basalts along the Endeavour segment, may make this location especially suited to large amounts of barite forming in plume. In turn, this could explain the observation of Baker and Massoth [1987] that in the Endeavour plume light attenuation correlates strongly with the S, but not Fe, content of the plume particles.

### 3.2.3. Pb-Isotopes

The Pb-isotopic composition of the sediments provides insight into the sources of Pb in the samples because the Endeavour basalts have different Pb-isotope ratios than surrounding sediments and the overlying ocean. The Pb-isotope data for the Endeavour sediments can be explained as simple mixtures of these components (Figure 9). For the Pb-isotopic composition of the hydrothermal end-member, we use sulfides from the Main Endeavour field [LeHuray *et al.*, 1988] rather than basalts both because these have the advantage of homogenizing any Pb-isotope heterogeneity within the basalts [e.g., Fouquet and Marcoux, 1995] and because of the possibility of a sediment contribution to the hydrothermal fluid [Lilley *et al.*, 1993; Butterfield *et al.*, 1994]. The Pb-isotopic composition of sediments from the Cascadia basin is significantly more radiogenic than the hydrothermal sulfides (Figure 9) [Carpentier *et al.*, 2014; Noguchi *et al.*, 2008]. The Pb-isotopic composition of deep Pacific seawater is taken from the Pb-isotopic composition of Mn

of the Pb in the samples comes from hydrothermal fluid, with the other two components making up  $\leq 15\%$  of the Pb.

The significant amount of seawater Pb in samples collected  $>1$  km from the vent fields, as indicated by elevated  $^{207}\text{Pb}/^{204}\text{Pb}$  and  $^{208}\text{Pb}/^{204}\text{Pb}$  at a given  $^{206}\text{Pb}/^{204}\text{Pb}$  (Figure 9 insets), provides insight into mixing and scavenging in the water column. For the samples far from vents, the offset to higher  $^{207}\text{Pb}/^{204}\text{Pb}$  and  $^{208}\text{Pb}/^{204}\text{Pb}$  at a given  $^{206}\text{Pb}/^{204}\text{Pb}$  suggests 5–10% more of the Pb in these samples comes from seawater relative to the samples closer to vents. The hydrothermal component of these samples has a Pb/FeO ratio of  $\sim 20$  (ppm/wt %). Given a vent fluid Fe content of  $\sim 1$  mmol  $\text{kg}^{-1}$  and a dilution factor in the plume of  $\sim 8000$ , scavenging all the Pb from the seawater in the plume (with  $\sim 10$  pmol  $\text{kg}^{-1}$  Pb) would give 2.3 ppm of seawater Pb per wt % of hydrothermal FeO; this is roughly 10% of the observed Pb/FeO. This back-of-the-envelope calculation broadly agrees with the suggestion from the Pb-isotope data that 5–10% of the Pb in these samples comes from seawater. It is also consistent with the high extent of Pb scavenging in the Endeavour plume determined based on depletion of dissolved  $^{210}\text{Pb}$  in the Endeavour plume by Kadko [1993].

### 3.2.4. Mn

High-temperature hydrothermal fluids along the Endeavour ridge contain significant amounts of Mn (70–550  $\mu\text{mol kg}^{-1}$ ) with the molar Mn/Fe ranging widely from 0.2 to 2.1 [Butterfield *et al.*, 1994; Seyfried *et al.*, 2003; Lin *et al.*, 2016]. Due to the slow, biologically mediated, kinetics of Mn oxidation in the water column sediments close to the vents are expected to be Mn-poor relative to those further from the vent [Lavelle *et al.*, 1992; Cowen *et al.*, 1990]. Furthermore, diagenetic processes mobilize Mn in the sediment column leading to the uppermost sediments generally being enriched in Mn relative to deeper sediments. This is exactly the pattern observed in the Endeavour sediments with MnO/FeO of the hydrothermal component increasing from  $<0.02$  in the sediment trap and near-vent sediment samples to as high as 0.3 in the most distal sediment samples (Figure 7). Most Mn (and even higher Mn/Fe sediment) is deposited much further off axis [e.g., Lavelle *et al.*, 1992].

### 3.2.5. P, V, As, REE, and U

Particles in the hydrothermal plume, in particular Fe-oxyhydroxides, are thought to scavenge elements from the water column potentially leading to a significant sink of some elements from the ocean (e.g., P, V, As, and REE, as well as Pb as discussed above) [German *et al.*, 1990; Feely *et al.*, 1991, 1998]. In the hydrothermal component of the sediments, Fe correlates strongly with As and P, consistent with scavenging of these elements from seawater onto Fe-oxyhydroxides being an important process. Superimposed on this gross correlation with Fe, the As/Fe ratio of the hydrothermal component varies systematically with distance from the vents being most enriched far from the vents and close to the vents with a minimum in between (Figure 7). The high As/Fe in near-vent sediments probably reflects accumulation of hydrothermal As bearing sulfides, as described above for elements like Ag and Cu [e.g., Breier *et al.*, 2012]; the much higher As/Fe of chimney material than any sediments is consistent with early precipitation of As in sulfides (Figure 7). Plume particles from the Endeavour segment have higher As/FeO ( $\sim 18$  ppm/wt %) and  $\text{P}_2\text{O}_5/\text{FeO}$  ( $\sim 0.2$  wt %/wt %) than the hydrothermal component of any of the sediments [Feely *et al.*, 1991]. Similar differences were observed in a sediment core from the EPR by Schaller *et al.* [2000] who suggested that As and P are lost, relative to Fe, during particle settling and early diagenetic processes. Alternatively, particles that settle the slowest, and hence are likely to be sampled as plume particles, may have higher As/Fe and P/Fe than larger particles that may contribute more of the mass of these elements into the sediments. For example, larger iron-oxyhydroxides would have larger mass to surface area and hence surface absorption would contribute less to their bulk composition. These differences in plume particle and sediment compositions have important implications for determining net fluxes from the ocean.

The V/Fe of the sediment core and sediment trap samples show no systematic variation with distance from the hydrothermal vents (Figure 7) with most sediments having V/Fe between that of the sediment trap samples and plume particulates (V/Fe  $\sim 16$ ) [Feely *et al.*, 1992]. However, Dymond and Roth [1988] report much higher V/Fe in their sediment trap samples (by roughly an order of magnitude), a difference that we cannot explain. Why V, which is generally thought to behave like other oxyanions such as As and P in hydrothermal plumes [e.g., German and Seyfried, 2014], shows this differing behavior is unclear.

The REEs (excluding Ce and Eu) are known to be scavenged from seawater onto particulate matter in hydrothermal plumes [e.g., Ruhlin and Owen, 1986; Barrett and Jarvis, 1988; German *et al.*, 1990; Sherrell

*et al.*, 1999]. This process is evident in the REE/Fe of the hydrothermal component in the sediments that increases with distance from the vents (Figure 7). The increase in REE/Fe with distance likely reflects a combination of an increasing fraction of the Fe that settled into the sediments coming from REE-rich Fe-oxyhydroxides rather than REE-poor sulfides and increased scavenging of REEs onto Fe-oxyhydroxides the longer they remain in the water column (either due to kinetic processes or increased availability of seawater REEs with increased dilution of the plume) [German *et al.*, 1990; Sherrell *et al.*, 1999]. The similar REE/Fe in the near-vent and sediment trap samples, and the systematic change in REE/Fe with distance from the vents, suggests that post deposition scavenging of REEs is insufficient to mask these primary depositional signals.

Uranium is enriched in the sediments close to the vent fields (up to >10 ppm) with U/Fe decreasing over a few hundred meters from the vents. Since U is depleted relative to seawater in vent fluids [e.g., Seyfried *et al.*, 2003], this U enrichment is most easily explained as due to uptake of seawater U most likely due to reduction of dissolved  $U^{6+}$  to immobile  $U^{4+}$  during sulfide oxidation [e.g., Mills *et al.*, 1994]. Sulfide mineral oxidation may occur both in the water column and on the seafloor.

### 3.3. A Simple Mass Balance for the Endeavour Hydrothermal Plume

In this section, we use the sediment geochemistry to calculate the fluxes of elements out of the water column associated with the hydrothermal plume within the first 1.5 km from the major vent fields. This is the approximate separation of the vent fields along the Endeavour segment. The calculated hydrothermal mass accumulation rate decreases from  $\sim 13 \text{ g m}^{-2} \text{ yr}^{-1}$  in the sediment trap to  $\sim 2 \text{ g m}^{-2} \text{ yr}^{-1}$  1500 m from the vents and even lower 3 km off axis (Figure 6). As a first approximation, we fit a power law curve through the calculated hydrothermal mass accumulation rate that is forced through the average sediment trap mass accumulation rate ( $13.2 \text{ g m}^{-2} \text{ yr}^{-1}$ )—this gives an average hydrothermal mass accumulation rate of  $3.1 \text{ g m}^{-2} \text{ yr}^{-1}$  from 0 to 1500 m from the vents.

The results of the tow-yo survey (Figure 2), and previous water column surveys [Baker and Massoth, 1987; Thomson *et al.*, 1992, 2003, 2005], suggest that the hydrothermal plume transports material along axis and onto the west flank with a much smaller flux onto the east flank. However, mixing within the  $\sim 1000 \text{ m}$  wide axial valley (Figure 1) probably reduces or eliminates this preferred westward transport of hydrothermal sediment close to the vents. Thus, to convert the linear change of sedimentation rate into a total mass accumulation rate, we assume that the variation in hydrothermal mass accumulation rate shown in Figure 6 is true for somewhere between a circle around the vents and a semicircle extending along axis and out to the west flank but not the east flank. Integrating the total mass accumulation from 0 to 1500 m from the vents in this way gives a hydrothermal sediment mass accumulation rate of between 9200 and 18,400  $\text{kg yr}^{-1}$  per 3 km along axis (i.e., roughly per vent field). These near-vent sediment mass accumulation rates are smaller than, but of the same order of magnitude as, the maximum mass accumulation rates for the hydrothermal chimney deposits of  $\sim 50\text{--}75,000 \text{ kg yr}^{-1}$  per vent field [Jamieson *et al.*, 2014].

The same approach is used to estimate the chemical fluxes into the sediments within 1.5 km of the major vent fields using the “hydrothermal component” mass accumulation rates just described and splines fit through the composition of the “hydrothermal component” as a function of distance from the vents. We emphasize that these are rough estimates but the results allow first order interpretations to be made about the transport away from the axis of even the most insoluble elements in the hydrothermal fluid. The aerally integrated accumulation rate for iron is between 29 and  $58 \times 10^3 \text{ mol yr}^{-1}$ . It is informative to compare this to an estimate of the Fe vented into the ocean. Assuming a heat flux of  $\sim 420 \text{ MW}$  per vent field along the Endeavour segment [Baker, 2007], and  $\sim 50\%$  of this vented at high-temperature with a fluid enthalpy of  $\sim 2000 \text{ kJ kg}^{-1}$  and an Fe content of  $\sim 800 \mu\text{mol kg}^{-1}$  [Butterfield *et al.*, 1994; Seyfried *et al.*, 2003; Bao *et al.*, 2008; Lin *et al.*, 2015],  $2.6 \times 10^6 \text{ mol yr}^{-1}$  of Fe are vented. This back-of-the-envelope calculation suggests that on the order of 1% of the Fe vented is deposited within 1.5 km of the major vent fields. Even accounting for the substantial uncertainties in the input parameters it is clear the vast majority of the Fe vented into the ocean is transported  $\gg 1.5 \text{ km}$  from the vent fields. Accumulation rates for other elements that are enriched in vent fluids over seawater and are highly insoluble in the ocean (Cd, Ag, Cu, and Pb) were calculated in the same way as for Fe. In all cases,  $<2\%$  of the flux vented into the oceans appears to have accumulated within sediments deposited with 1.5 km of the vent fields. Thus, along the Endeavour segment the vast majority of even the least soluble elements are exported  $>1.5 \text{ km}$ .



The observation that the mass accumulation rate of the hydrothermal component decreases rapidly with distance from the vents (Figure 6), while most of the hydrothermal component remains in the water column, is informative. The rapid decrease in mass accumulation rate of the hydrothermal component within hundreds of meters of the major vents probably reflects the rapid sedimentation of sulfides and sulfates in this region. However, even in this high  $\text{H}_2\text{S}/\text{Fe}$  system only a small fraction of the chalcophile elements are stripped from the plume in this near-vent region. Further from the vents much slower sedimentation of Fe-oxyhydroxides and Mn-oxyhydroxides (and elements coprecipitated with these and scavenged by them) leads to widespread dispersal of the hydrothermal component. Thus, changes in the mineralogy of the particulates forming in the water column, and their rate of precipitation and sedimentation, are likely to be more important in controlling the bulk composition of near ridge hydrothermal sediments than the absolute hydrothermal flux.

#### 4. Conclusions

Processes operating in the hydrothermal plume above the Endeavour vents have been investigated using both water column observations and sediment geochemistry. Comparison of the thermal and light attenuation anomalies in the water column suggest that about half of the heat flux comes from particulate-poor diffuse flow. This is less than is generally suggested implying that there may be less subsurface mixing and element precipitation than is generally assumed. Hence a larger fraction of the highly insoluble elements may be vented into the ocean rather than precipitated within the subsurface.

Early sulfide precipitation within the water column leads to enrichment of the near-vent sediments in chalcophile elements with the relative order of enrichment being  $\text{Cd} > \text{Ag} > \text{Cu} > \text{Co} \sim \text{Fe}$  similar to the order of enrichment in the chimneys over the near-vent sediments. Barite, and perhaps other sulfate minerals, have a peak in sedimentation a little further from the vents leading to a peak in the accumulation rates of Ba, Sr, and Pb. Iron and Mn oxides and oxyhydroxide formation leads to substantial scavenging of elements like REE and Pb from the water column. Despite strong geochemical signals of the accumulation of insoluble elements that are strongly enriched in hydrothermal fluids over seawater, sedimentation within 1.5 km of the vents removes at most a few percent of the hydrothermal flux into the ocean. The transport of much of the particulate and dissolved flux significant distances away from the ridge axis region is consistent with enhanced accumulation of hydrothermally sourced metals in seafloor sediments for millions of years after crustal formation [e.g., Dymond *et al.*, 1977; Barrett *et al.*, 1987]. In turn, this indicates that changes in near-axis hydrothermal sediment accumulation rate may be just as susceptible to changes in particle formation and sedimentation rates as they are to changes in hydrothermal fluxes.

#### Acknowledgments

Support from ONC for sample collection is gratefully acknowledged as is the analytical expertise of Jody Spence, Bruno Keiffer, and Maureen Soon who helped generate the data set reported here. Funding for sample analysis came from an NSERC Discovery Grant to L.A.C. Ocean Networks Canada is supported through the Canadian Foundation for Innovation. All data are provided in the supporting information or through ONC at <http://dmas.uvic.ca/DataSearch>.

#### References

- Antao, S. (2012), Structural trends for celestite ( $\text{SrSO}_4$ ), anglesite ( $\text{PbSO}_4$ ), and barite ( $\text{BaSO}_4$ ): Confirmation of expected variations within the  $\text{SO}_4$  groups, *Am. Mineral.*, *97*, 661–665.
- Baker, E. T., and G. J. Massoth (1987), Characteristics of hydrothermal plumes from two vent fields on the Juan de Fuca Ridge, northeast Pacific Ocean, *Earth Planet. Sci. Lett.*, *85*, 59–73.
- Baker, E. T. (2007), Hydrothermal cooling of mid-ocean ridges axes: do measured and modeled heat fluxes agree?, *Earth Planet. Sci. Lett.*, *263*, 140–150.
- Bao, S.-X., H.-Y. Zhou, X.-T. Peng, F.-W. Ji, and H.-Q. Yao (2008), Geochemistry of REE and yttrium in hydrothermal fluids from the Endeavour segment, Juan de Fuca Ridge, *Geochem. J.*, *42*, 359–370.
- Barrett, T. J., and I. Jarvis (1988), Rare-earth element geochemistry of metalliferous sediments from DSDP Leg 92: The East Pacific Rise transect, *Chem. Geol.*, *67*, 243–259.
- Barrett, T. J., P. N. Taylor, and J. Lugooski (1987), Metalliferous sediments from DSDP Leg 92: The East Pacific Rise transect, *Geochim. Cosmochim. Acta*, *51*, 2241–2253.
- Breier, J. A., B. M. Toner, S. C. Fakra, M. A. Marcus, S. N. White, A. M. Thurnherr, and C. R. German (2012), Sulfur, sulfides, oxides and organic matter aggregated in submarine hydrothermal plumes at 9°50'N East Pacific Rise, *Geochim. Cosmochim. Acta*, *88*, 216–236.
- Butterfield, D. A., R. E. McDuff, M. J. Mottl, M. D. Lilley, J. E. Lupton, and G. J. Massoth (1994), Gradients in the composition of hydrothermal fluids from the endeavor segment vent field: Phase-separation and brine loss, *J. Geophys. Res.*, *99*, 9561–9583.
- Carpentier, M., D. Weis, and C. Chauvel (2013), Large U loss during weathering of upper continental crust: The sedimentary record, *Chem. Geol.*, *340*, 91–104.
- Carpentier, M., D. Weis, and C. Chauvel (2014), Fractionation of Sr and Hf isotopes by mineral sorting in Cascadia Basin terrigenous sediments, *Chem. Geol.*, *380*, 67–82.
- Chin, C. S., K. H. Coale, V. A. Elrod, K. S. Johnson, G. J. Massoth, and E. T. Baker (1994), In situ observations of dissolved iron and manganese in hydrothermal vent plumes, Juan de Fuca Ridge, *J. Geophys. Res.*, *99*, 4969–4984.
- Clague, D. A., et al. (2014), Eruptive and tectonic history of the Endeavour Segment, Juan de Fuca Ridge, based on AUV mapping data and lava flow ages, *Geochem. Geophys. Geosyst.*, *15*, 3364–3391, doi:10.1002/2014GC005415.

- Coogan, L. A., and S. Dosso (2012), An internally consistent, probabilistic, determination of ridge-axis hydrothermal fluxes from basalt-hosted systems, *Earth Planet. Sci. Lett.*, **323**, 92–101.
- Cowen, J. P., G. J. Massoth, and R. A. Feely (1990), Scavenging rates of dissolved manganese in a hydrothermal vent plume, *Deep Sea Res., Part A*, **37**, 1619–1637.
- Dymond, J., and S. Roth (1988), Plume dispersed hydrothermal particles: A time-series record of settling flux from the Endeavour Ridge using moored sensors, *Geochim. Cosmochim. Acta*, **52**, 2525–2536.
- Dymond, J., J. B. Corliss, and G. R. Heath (1977), History of metalliferous sedimentation at deep sea drilling site 319 in the South Eastern Pacific, *Geochim. Cosmochim. Acta*, **41**, 741–753.
- Edmond, J. M., C. Measures, R. E. McDuff, L. H. Chan, R. Collier, B. Grant, L. I. Gordon, and J. B. Corliss (1979), Ridge crest hydrothermal activity and the balances of the major and minor elements in the ocean: The Galapagos data, *Earth Planet. Sci. Lett.*, **46**, 1–18.
- Elderfield, H., and A. Schultz (1996), Mid-ocean ridge hydrothermal fluxes and the chemical composition of the ocean, *Annu. Rev. Earth Planet. Sci.*, **24**, 191–224.
- Feely, R. A., M. Lewison, G. J. Massoth, G. Robert-Baldo, J. W. Lavelle, R. H. Byrne, K. L. Von Damm, and H. C. Curl (1987), Composition and dissolution of black smoker particulates from active vents on the Juan de Fuca Ridge, *J. Geophys. Res.*, **92**, 11,347–11,363.
- Feely, R. A., J. H. Trefry, G. J. Massoth, and S. Metz (1991), A comparison of the scavenging of phosphorus and arsenic from seawater by hydrothermal iron oxyhydroxides in the Atlantic and Pacific Oceans, *Deep Sea Res., Part A*, **38**, 617–623.
- Feely, R. A., G. J. Massoth, E. T. Baker, G. T. Lebon, and T. L. Geiselman (1992), Tracking the dispersal of hydrothermal plumes from the Juan de Fuca Ridge using suspended matter compositions, *J. Geophys. Res.*, **97**, 3457–3468.
- Feely, R. A., J. H. Trefry, G. T. Lebon, and C. R. German (1998), The relationship between P/Fe and V/Fe ratios in hydrothermal precipitates and dissolved phosphate in seawater, *Geophys. Res. Lett.*, **25**, 2253–2256.
- Field, M. P., and R. M. Sherrell (2000), Dissolved and particulate Fe in a hydrothermal plume at 9°45'N, East Pacific Rise: Slow Fe (II) oxidation kinetics in Pacific plumes, *Geochim. Cosmochim. Acta*, **64**, 619–628.
- Fouquet, Y., and E. Marcoux (1995), Lead isotope systematics in Pacific hydrothermal sulfide deposits, *J. Geophys. Res. Solid Earth*, **100**(B4), 6025–6040, doi:10.1029/94JB02646.
- German, C. R., and W. E. Seyfried Jr. (2014), 8.7 Hydrothermal processes, in *Treatise on Geochemistry*, 2nd ed., edited by H. D. Holland and K. K. B. Turekian, pp. 191–233, Elsevier, Oxford, U. K.
- German, C. R., G. P. Klinkhammer, J. M. Edmond, A. Mura, and H. Elderfield (1990), Hydrothermal scavenging of rare-earth elements in the ocean, *Nature*, **345**, 516–518.
- German, C. R., J. Hergt, M. R. Palmer, and J. M. Edmond (1999), Geochemistry of a hydrothermal sediment core from the OBS vent-field, 21°N East Pacific Rise, *Chem. Geol.*, **155**, 65–75.
- Germanovich, L. N., R. S. Hurt, J. E. Smith, G. Genc, and R. P. Lowell (2015), Measuring fluid flow and heat output in seafloor hydrothermal environments, *J. Geophys. Res. Solid Earth*, **120**, 8031–8055, doi:10.1002/2015JB012245.
- Hannington, M. D., S. Petersen, P. M. Herzig, and I. R. Jonasson (2004), A global database of seafloor hydrothermal systems, including a digital database of analyses of seafloor polymetallic sulfides [1 CD-ROM], *Geol. Surv. Can. Open File*, **4598**, Ottawa, Canada.
- Hrischeva, E., and S. D. Scott (2007), Geochemistry and morphology of metalliferous sediments and oxyhydroxides from the Endeavour segment, Juan de Fuca Ridge, *Geochim. Cosmochim. Acta*, **71**, 3476–3497.
- Jamieson, J. W., M. D. Hannington, D. A. Clague, D. S. Kelley, J. R. Delaney, J. F. Holden, M. K. Tivey, and L. E. Kimpfe (2013), Sulfide geochronology along the Endeavour Segment of the Juan de Fuca Ridge, *Geochem. Geophys. Geosyst.*, **14**, 2084–2099, doi:10.1002/ggge.20133.
- Jamieson, J. W., D. A. Clague, and M. D. Hannington (2014), Hydrothermal sulfide accumulation along the Endeavour Segment, Juan de Fuca Ridge, *Earth Planet. Sci. Lett.*, **395**, 136–148.
- Jamieson, J. W., et al. (2016), Precipitation and growth of barite within hydrothermal vent deposits from the Endeavour Segment, Juan de Fuca Ridge, *Geochim. Cosmochim. Acta*, **173**, 64–85.
- Kadko, D. (1993), An assessment of the effect of chemical scavenging within submarine hydrothermal plumes upon ocean geochemistry, *Earth Planet. Sci. Lett.*, **120**, 361–374.
- Kelley, D. S., et al. (2012), Endeavour segment of the Juan de Fuca Ridge: One of the most remarkable places on Earth, *Oceanography*, **25**(1), 44–61.
- Kellogg, J. P., and R. E. McDuff (2010), A hydrographic transient above the Salty Dawg hydrothermal field, Endeavour segment, Juan de Fuca Ridge, *Geochem. Geophys. Geosyst.*, **11**, Q12001, doi:10.1029/2010GC003299.
- Kristall, B., D. Nielsen, M. D. Hannington, D. S. Kelley, and J. R. Delaney (2011), Chemical microenvironments within sulfide structures from the Mothra Hydrothermal Field: Evidence from high-resolution zoning of trace elements, *Chem. Geol.*, **290**(1–2), 12–30, doi:10.1016/j.chemgeo.2011.08.008.
- Lavelle, J. W., J. P. Cowen, and G. J. Massoth (1992), A model for the deposition of hydrothermal manganese near ridge crests, *J. Geophys. Res.*, **97**, 7413–7427.
- LeHuray, A. P., S. E. Church, R. A. Koski, and R. M. Bouse (1988), Pb isotopes in sulfides from mid-ocean ridge hydrothermal sites, *Geology*, **16**, 362–365.
- Lilley, M. D., D. A. Butterfield, E. J. Olson, J. E. Lupton, S. A. Macko, and R. E. McDuff (1993), Anomalous CH<sub>4</sub> and NH<sub>4</sub><sup>+</sup> concentrations at an unsedimented mid-ocean-ridge hydrothermal system, *Nature*, **364**, 45–47.
- Lilley, M. D., R. A. Feely, and J. H. Trefry (1995), Chemical and biological transformations in hydrothermal plumes, in *Seafloor Hydrothermal Systems: Physical, Chemical, Biological, and Geological Interactions*, edited by S. E. Humphris et al., pp. 369–391, AGU, Washington, D. C.
- Lin, T. J., et al. (2016), Linkages between mineralogy, fluid chemistry, and microbial communities within hydrothermal chimneys from the Endeavour Segment, Juan de Fuca Ridge, *Geochem. Geophys. Geosyst.*, **17**, 300–323, doi:10.1002/2015GC006091.
- Mills, R. A., J. Thomson, H. Elderfield, R. W. Hinton, and E. Hyslop (1994), Uranium enrichment in metalliferous sediments from the Mid-Atlantic Ridge, *Earth Planet. Sci. Lett.*, **124**, 35–47.
- Mottl, M. J., and T. F. McConachy (1990), Chemical processes in buoyant hydrothermal plumes on the East Pacific Rise near 21°N, *Geochim. Cosmochim. Acta*, **54**, 1911–1927.
- Noguchi, T., R. Shinjo, and T. Oomori (2008), Data report: Pb isotope compositions of sediment from the eastern flank of Juan de Fuca Ridge, in *Proc. Integrated Ocean Drill. Program*, vol. 301, edited by A. T. Fisher et al., Integr. Ocean Drill. Program Manage. Int., College Station, Tex., doi:10.2204/iodp.proc.301.203.2008.
- Rona, P. A., and D. A. Trivett (1992), Discrete and diffuse heat transfer atashes vent field, Axial Volcano, Juan de Fuca Ridge, *Earth Planet. Sci. Lett.*, **109**, 57–71.

- Rudnicki, M. D., and H. Elderfield (1993), A chemical model of the buoyant and neutrally buoyant plume above the TAG vent field, 26°N, Mid-Atlantic Ridge, *Geochim. Cosmochim. Acta*, *57*, 2939–2957.
- Ruhlin, D. E., and R. M. Owen (1986), The rare earth element geochemistry of hydrothermal sediments from the East Pacific Rise: Examination of a seawater scavenging mechanism, *Geochim. Cosmochim. Acta*, *50*, 393–400.
- Schaller, T., J. Morford, S. R. Emerson, and R. A. Feely (2000), Oxyanions in metalliferous sediments: Tracers for paleoseawater metal concentrations?, *Geochim. Cosmochim. Acta*, *64*, 2243–2254.
- Schultz, A., J. R. Delaney, and R. E. McDuff (1992), On the partitioning of heat flux between diffuse and point source seafloor venting, *J. Geophys. Res.*, *97*, 12,212–299,314.
- Seyfried, W. E., J. S. Seewald, M. E. Berndt, K. Ding, and D. I. Foustoukos (2003), Chemistry of hydrothermal vent fluids from the Main Endeavour Field, northern Juan de Fuca Ridge: Geochemical controls in the aftermath of June 1999 seismic events, *J. Geophys. Res.*, *108*(B9), 2429, doi:10.1029/2002JB001957.
- Sherrell, R. M., M. P. Field, and G. Ravizza (1999), Uptake and fractionation of rare earth elements on hydrothermal plume particles at 9°45'N, East Pacific Rise, *Geochim. Cosmochim. Acta*, *63*, 1709–1722.
- Thomson, R. E., B. J. Burd, A. G. Dolling, R. Lee Gordon, and G. S. Jamieson (1992), The deep scattering layer associated with the Endeavour Ridge hydrothermal plume, *Deep Sea Res., Part A*, *39*, 55–73.
- Thomson, R. E., S. F. Mihal, A. B. Rabinovich, R. E. McDuff, S. R. Veirs, and F. R. Stahr (2003), Constrained circulation at Endeavour ridge facilitates colonization by vent larvae, *Nature*, *424*, 545–549.
- Thomson, R. E., M. M. Subbotina, and M. V. Anisimov (2005), Numerical simulation of hydrothermal vent-induced circulation at Endeavour Ridge, *J. Geophys. Res.*, *110*, C01004, doi:10.1029/2004JC002337.
- Veirs, S. R., R. E. McDuff, and F. R. Starr (2006), Magnitude and variance of near-bottom horizontal heat flux at the Main Endeavour hydrothermal vent field, *Geochem. Geophys. Geosyst.*, *7*, Q02004, doi:10.1029/2005GC000952.
- von Blanckenburg, F., R. K. O'Nions, and J. R. Heinz (1996), Distribution and sources of pre-anthropogenic lead isotopes in deep ocean water from FeMn crusts, *Geochim. Cosmochim. Acta*, *60*, 4957–4963.
- Von Damm, K. L. (1995), Controls on the chemistry and temporal variability of seafloor hydrothermal fluids, in *Seafloor Hydrothermal Systems: Physical, Chemical, Biological, and Geological Interactions*, edited by S. E. Humphris et al., pp. 222–247, AGU, Washington, D. C.
- Weis, D., et al. (2006), High-precision isotopic characterization of USGS reference materials by TIMS and MC-ICP-MS, *Geochem. Geophys. Geosyst.*, *7*, Q08006, doi:10.1029/2006GC001283.

## Erratum

In the originally published version of this article, Figure 4 was missing the figure legend. The figure has since been updated, and this version may be considered the authoritative version of record.